Acoustic Energy Exchange Between Frequencies During Non-Linear Propagation of Shock Waves

Majd Daroukh, Cyril Polacsek, Thomas Le Garrec, Jordan Thisse, Thomas Nodé-Langlois, Ricardo Blazquez

To cite this version:

Majd Daroukh, Cyril Polacsek, Thomas Le Garrec, Jordan Thisse, Thomas Nodé-Langlois, et al.. Acoustic Energy Exchange Between Frequencies During Non-Linear Propagation of Shock Waves. AIAA-CEAS Aeroacoustics Conference 2024, Jun 2024, Rome, Italy. 10.2514/6.2024-3424 . hal-04921702

HAL Id: hal-04921702
https://hal.science/hal-04921702v1

Submitted on 30 Jan 2025

Acoustic energy exchange between frequencies during non-linear propagation of shock waves

M. Daroukh*, C. Polacsek and T. Le Garrec
DAAA, ONERA, Institut Polytechnique de Paris
92320 Châtillon, France

J. Thisse, T. Nodé-Langlois and R. Blazquez Navarro
Airbus Operations
31300 Toulouse, France

In a previous paper dedicated to the validation of a numerical methodology to predict shock wave generation and propagation from the ACAT1 fan stage, unexpected variations of the power levels associated with the blade passing frequencies were observed inside the duct. Such variations are theoretically possible due to the non-linearity of the propagation of shock waves, but their amplitude and their localization close to the duct exit were uncommon. This phenomenon is further investigated in this paper using two different computational aeroacoustic solvers. The effects of duct geometry, non-linearity of the equations, and injection data are investigated. The results show that these power level variations are due to non-linear effects combined with the heterogeneity of the mean flow. When the input signal is prescribed frequency by frequency, these variations become minor. An interesting observation is that the complete result obtained when injecting all frequencies together is recovered when injecting only the dominant frequency due to the diffusion over its harmonics by non-linear effects.

I. Introduction

The shocks that develop over fan blade suction sides at transonic speeds are an important contributor to aircraft tonal noise. This noise source can be captured by computational fluid dynamics (CFD) simulations in a one-step approach by computing simultaneously the generation and the propagation of shock waves [1–3]. However, this approach remains computationally expensive in general, and a two-step methodology is often required with the capture of shock generation by a CFD solver, and the propagation of shock waves by a computational aeroacoustics (CAA) solver [4–7]. A validation of the latter methodology on the ACAT1 fan stage from the TurboNoiseBB European project [8] has recently been proposed by the authors [9] with the assumption of perfectly identical blades i.e. without including multiple pure tones (MPTs). The CFD/CAA chaining strategy developed by Thisse *et al.* [10] where the shocks are injected into the CAA domain in terms of usual conservative variables using a non-reflecting boundary condition has been used. Despite an excellent behaviour of the chaining strategy and acceptable comparisons against experiments, unexpected variations of the sound power levels associated with the blade passing frequencies (BPFs) were observed inside the duct. The total acoustic power effectively reaches a plateau after a certain distance from the source, but the contribution of the BPFs to this total acoustic power kept varying. The phenomenon in the case of a perfect fan without MPTs has not been reported yet in the literature to the authors knowledge, and the present paper aims to further investigate it.

To this end, we first highlight these variations by applying the same CFD/CAA methodology with ONERA's solver *elsA* as in the previous study [9]. In addition to the nominal point (100% engine speed) of the latter study [9], a point at a lower regime (93.5% speed) where the phenomenon is emphasized is also computed. Then, we repeat the propagation step (the input shock signature is unchanged) by considering successive simplifications of the geometry (and therefore flow) to evaluate how this exchange of energy between frequencies is impacted. Further investigations are then reported for one of these geometries. In particular, the results obtained with *elsA* are compared against the solutions provided by the solver *sAbrinA* which either solves the linearized or non-linearized Euler equations. The latter capacity is then used to specifically evaluate the effect of the non-linearity of the governing equations. Finally, the results obtained when the input signal is specified frequency by frequency are addressed.

The two solvers used for propagating shock waves in this study are first presented in Sec. II. The unexpected acoustic power variations observed on the ACAT1 fan stage are then discussed in Sec. III, along with the description of the case.

---

*Corresponding author: majd.daroukh@onera.fr

Next, the effect of duct geometry on these variations is evaluated in Sec. IV. Finally, the particular case with constant hub radius is further analyzed in Sec. V while Sec. VI adresses the main conclusions.

II. Description of numerical methodology

A. Overview

The configuration of interest in this paper is derived from the ACAT1 fan stage [11, 12], a transonic fan that has been tested in the Universal Fan Facility for Acoustics (UFFA) rig of AneCom AeroTest GmbH (Wildau, Germany)* during the TurboNoiseBB European project. The fan is composed of $B = 20$ blades with a radius R of about 0.45 m and the distance L from the fan plane to the inlet plane is approximately 1.2 m. Two operating points are considered in the current study: the nominal operating point (100% rotation speed) where the relative tip Mach number is equal to 1.21, and a point at a lower regime (93.5% of rotation speed) where the relative tip Mach number is equal to 1.12. Note that all distances are made dimensionless in the presented results by dividing them by the intake length.

An overall CFD/CAA methodology has been validated at nominal conditions against the experimental far-field acoustic results (obtained from 25 microphones equally placed over an arc of radius 18.5 m centered on the fan plane from 0 to 120 deg) in a previous dedicated paper [9]. In the current paper, only the propagation step of the methodology is repeated (particularly by simplifying the geometry) to understand the cause of the observed exchange of acoustic energy between frequencies. In addition to the *elsA* solver used in the original methodology [9], the *sAbrinA* solver [13] is also used here for benchmarking and additional analyses.

B. elsA simulations

The v5.1.03 version of *elsA* solver (ONERA-Safran property) [14], based on a cell-centered finite volume approach on a structured multiblock grid, is used in Euler mode in this paper to propagate shock waves from an initial shock signature using the chaining strategy developed by Thisse *et al.* [10]. All configurations addressed in this study are axisymmetric so that the steady Euler equations can be solved in the relative frame. The link between time t and azimuthal angle θ ($\theta = \Omega t$ with Ω the rotation speed) is used to reconstruct the unsteady fields in the fixed frame from steady values in the rotating domain. The implicit backward Euler time scheme and the Roe spatial scheme with van Albada limiter are used. The input shock signature (e.g. extracted from the CFD simulation) is specified in terms of conservative variables using Thompson's non-reflecting boundary condition based on 1-D characteristic equations [15]. Only one sector is modeled ($2\pi/20$ azimuthal extent) and periodic boundary conditions are specified on azimuthal boundaries. All walls are considered as frictionless. For cases including the nacelle inlet, non-reflecting boundary conditions are specified on far-field boundaries, while for cases restricted to the in-duct domain, a classic injection condition (where total enthalpy, total pressure and velocity direction are prescribed) is used. The baseline meshes are defined such that there is at least 30 points per wavelength associated with BPF3 in the axial direction (accounting for convective effects), 121 points in the azimuthal direction to describe one sector and 253 points in the radial direction. For the particular configuration studied in Sec. V, a fine mesh with twice the number of points in the axial and azimuthal directions is also considered.

C. sAbrinA simulations

In addition to *elsA* simulations, the ONERA's CAA solver *sAbrinA* [13], which solves through finite differences the linearized or non-linearized Euler equations in the time domain on a structured multi-block grid, is also used. The numerical resolution is here limited to the perturbation variables which are therefore uncoupled from the input base flow provided by the previous *elsA* simulations. This will permit to determine the impact of non-linearity on the energy exchange between BPFs, while forbidding any interaction between the mean flow and the acoustics. As the solver is unsteady by nature, the unsteady Euler equations are directly solved in the absolute frame. An azimuthal average of the flow computed by *elsA* (in the relative frame) is therefore performed to get the average base flow in the absolute frame. The input shock signature is decomposed into Fourier-Bessel modes (using the local geometry and flow values) that are prescribed in the source plane using a source model that allows back-running waves to cross the source without reflection [16, 17]. Additional simulations with a more advanced CFD/CAA chaining strategy based on the conservative variables [18] have led to quasi identical results and are not shown in this paper for concision reasons. As for *elsA* simulations, periodic conditions are used on azimuthal boundaries (one sector modeling) and all walls are considered as

---

*`https://www.anecom.de/services/aerodynamic-testing/fan-noise-and-performance-test/`

frictionless. Only the in-duct configuration with constant hub radius is computed with *sAbrinA*. The baseline mesh is built with at least 15 points per wavelength associated with BPF3 in the axial direction (accounting for convective effects), 46 points in the azimuthal direction to describe one sector and 121 points in the radial direction. A fine mesh with twice the number of points in the axial and azimuthal directions is also considered.

III. Observation of acoustic energy exchange between frequencies on the ACAT1 fan stage

In the previous related paper [9], a whole CFD/CAA chaining strategy has been applied on the ACAT1 fan stage at nominal operating conditions (100% rotation speed). The main results are recalled in Fig. 1, along with new ones obtained at a lower rotation speed (93.5%). The shock signature obtained by the CFD simulation (*elsA* solver) is represented in terms of contour maps of mean density in Figs. 1a and 1b. The shocks are characterized by significantly different angles as seen by their different azimuthal position in the map (while the blade position is unchanged) and stronger amplitudes are found in the lower speed case.

The mean flow resulting from the CAA simulations (with again *elsA* solver) fed by the previous shocks is illustrated by contour maps of axial Mach number in Figs. 1c and 1d. Based on the azimuthal angle / time analogy, these results are obtained on a meridional plane by computing the azimuthal average of the flow for each axial and radial position. Similar flow patterns are obtained between both operating conditions except that higher velocities are reached at nominal speed.

Qualitative acoustic results from these CAA simulations are then given in Figs. 1e and 1f which show contour maps of pressure real part at BPF2 over the meridional plane, obtained by computing the second azimuthal Fourier component of the pressure field for each axial and radial position (still based on the azimuthal angle / time analogy). As the acoustic field is only composed by the rotor-locked modes $m = sB$ (with m the azimuthal mode order and s the order of the considered BPF harmonic) of relative high orders, stronger pressure levels close to the casing are found inside the duct and the free-field radiation is mainly perpendicular to the axis. What retains our attention here are the regions where lower acoustic pressure levels are obtained, particularly near the inlet plane at 100% rotation speed and near $x/L = -0.7$ at 93.5% rotation speed.

These regions are better shown in Figs. 1g and 1h which give the evolution of in-duct acoustic power for BPF1-3. These curves are obtained by integrating over successive axial positions the acoustic intensity evaluated beforehand over the meridional plane using Cantrell and Hart formulation [19]. The total power, computed by summing the contributions from the first three BPFs is also provided. The two previous regions are indeed visible with very low power levels at BPF2 and BPF3. The effect is particularly dramatic at 93.5 % rotation speed with almost a complete extinction of acoustic pressure and acoustic power at BPF2 around $x/L = -0.7$. It is however important to note that, after a decay region that can be attributed to non-linear attenuation, the total power levels reach a plateau from $x/L = -0.5$ in both cases. The decrease of BPF2 and BPF3 power levels are indeed mitigated by an increase of BPF1 power level, which indicate an exchange of energy between these frequencies. These observations, while spectacular and never encountered by the authors, are therefore consistent with the fundamental principle that the acoustic energy must be conserved in a linear regime.

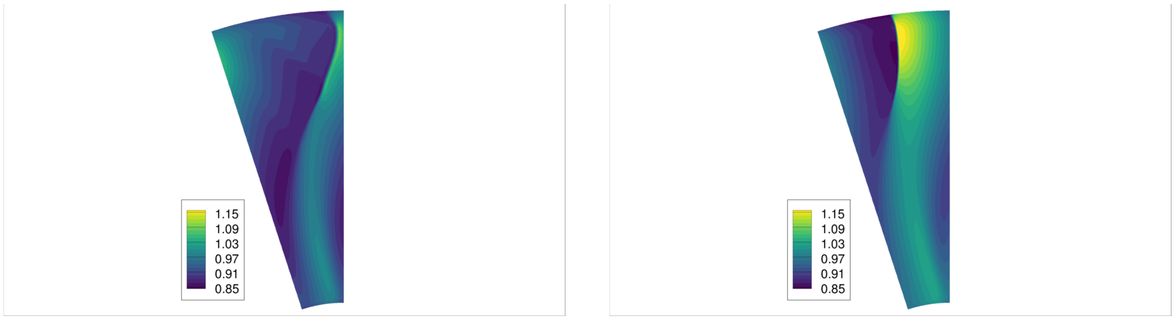

(a) Shock signature (mean density map in kg/m3) obtained from CFD - 100% speed

(b) Shock signature (mean density map in kg/m3) obtained from CFD - 93.5% speed.

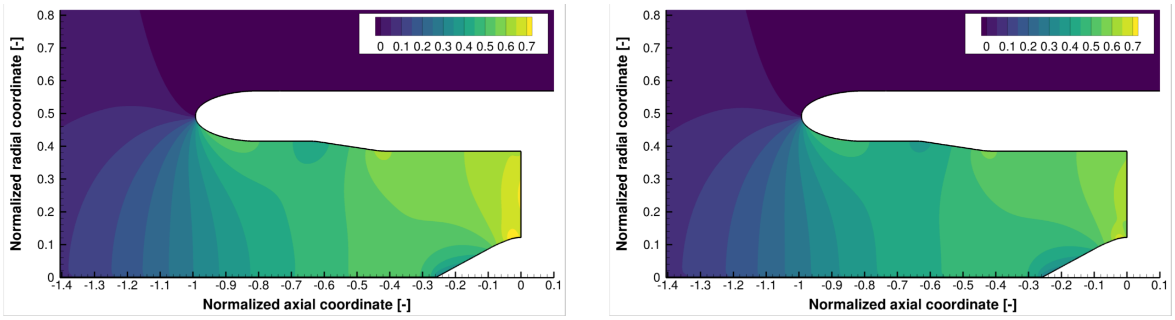

(c) Mean flow (axial Mach number map) obtained from CAA - 100% speed.

(d) Mean flow (axial Mach number map) obtained from CAA - 93.5% speed.

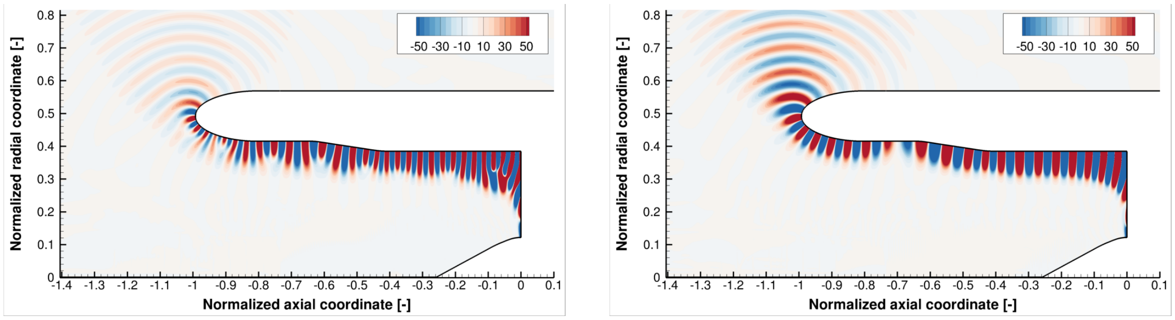

(e) Radiated pressure field at BPF2 (pressure real part map in Pa) - 100% speed.

(f) Radiated pressure field at BPF2 (pressure real part map in Pa) - 93.5% speed.

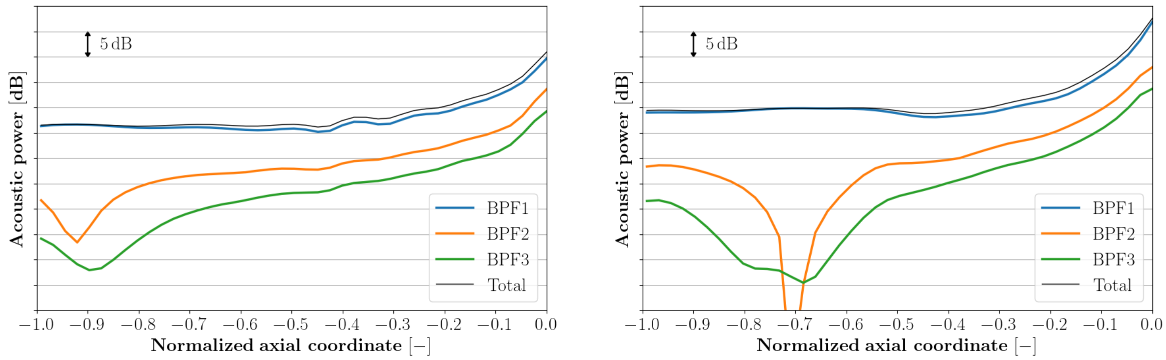

(g) Evolution of in-duct acoustic power (total and BPF contributions) - 100% speed.

(h) Evolution of in-duct acoustic power (total and BPF contributions) - 93.5% speed.

Fig. 1 Results using the methodology from [9] and applied to the ACAT1 fan stage at 93.5% and 100% of nominal speed.

IV. Effect of duct geometry on these acoustic energy exchange

In this section, we focus on the lower rotation speed case where the exchange of energy between frequencies is more pronounced, and we consider successive simplifications of the geometry to understand their origin. All the results presented in this section are obtained by repeating the propagation step using the *elsA* solver in Euler mode (see Sec. II.B), without changing the input shock signature.

A. Definition of simplified duct geometries

The different simplified geometries that are selected are shown in Fig. 2. The first simplification (Fig. 2a) consists in extending the original in-duct geometry from the nacelle leading edge by a straight duct to exclude any effect from the near-field. From this basis, three successive simplifications are made. The first one (Fig. 2b) consists in replacing the original tip line by a constant line while the second one (Fig. 2c) consists in similarly replacing the hub line. Finally, the third one (Fig. 2d) includes both simplifications and reduces to a simple straight duct.

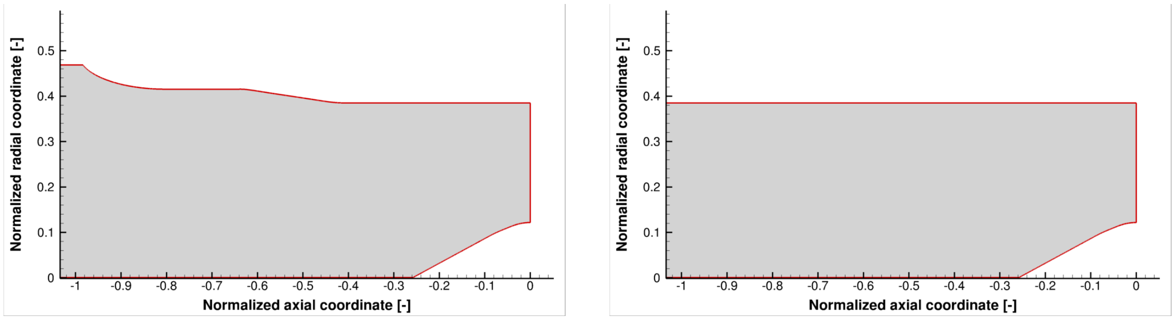

(a) Original duct geometry.

(b) Duct geometry with constant tip radius.

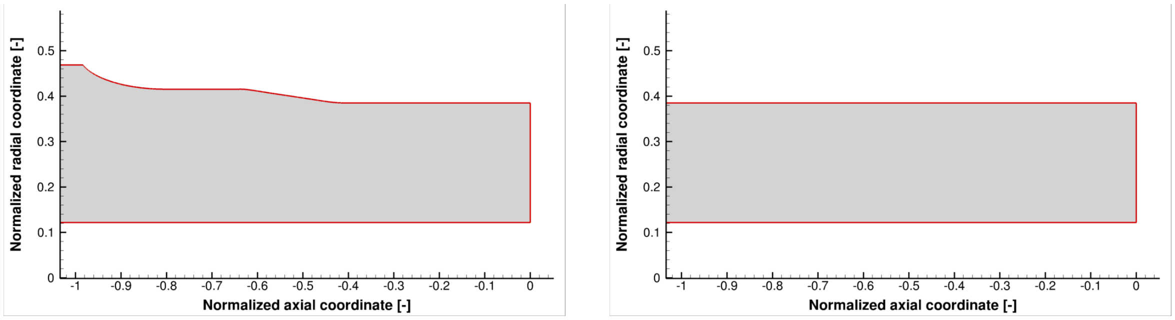

(c) Duct geometry with constant hub radius.

(d) Duct geometry with constant hub and tip radii.

Fig. 2 Definition of simplified duct geometries.

B. Mean flow results

The mean flow results obtained with each of these geometries are illustrated in Fig. 3 in terms of contour maps of axial Mach number. We can first notice that the mean flow obtained with the original geometry restricted to the in-duct domain (Fig. 3a) presents similar patterns as the ones observed with the original nacelle geometry (Fig. 1d). Consequently, this geometry simplification can be considered to isolate effects from the duct opening. When the tip line is defined at a constant radius (Fig. 3b), the mean flow heterogeneity is only caused by the spinner and the axial Mach number becomes almost uniform from $x/L = -0.4$. On the contrary, when the hub line is considered to be constant (Fig. 3c), the mean flow becomes particularly heterogeneous from $x/L = -0.4$ because of the tip line variations. The reduced cross-section area in this case also causes the mean flow velocity to be higher. Finally, when the duct is straight (Fig. 3d), the mean flow is obviously uniform. Some spots of heterogeneity are visible close to the injection plane ($x/L = 0$) because the input data was obtained with the real geometry and has not been recomputed.

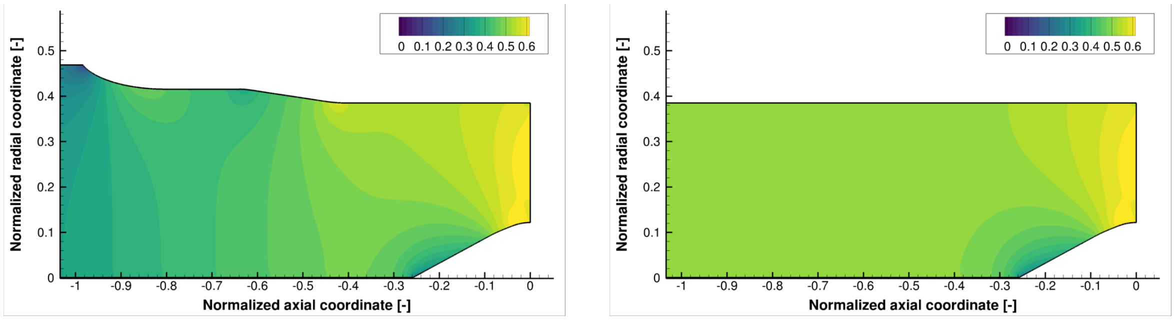

(a) Original duct geometry.

(b) Duct geometry with constant tip radius.

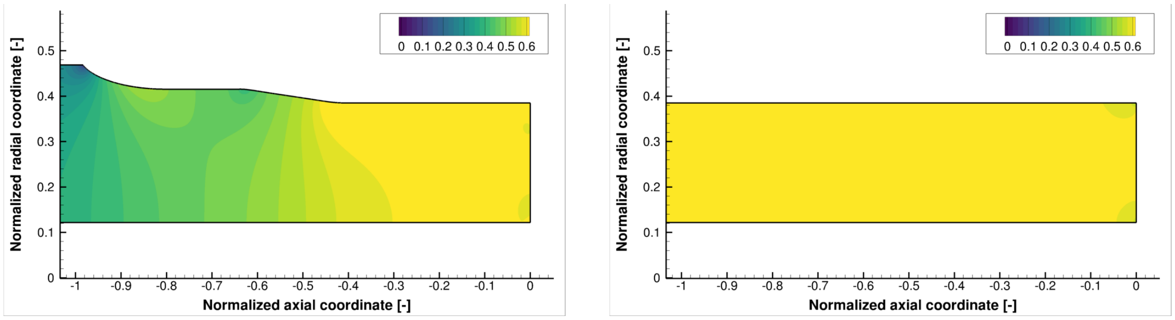

(c) Duct geometry with constant hub radius.

(d) Duct geometry with constant hub and tip radii.

Fig. 3 Contour maps of mean axial Mach number on meridional plane.

C. Acoustic results

Acoustic results from these simulations are now discussed. The contour maps of pressure real part at BPF2 along the meridional plane are given in Fig. 4. For a more quantitative assessment, the axial evolution of the acoustic power carried out by each BPF is also plotted in Fig. 5. For the original geometry restricted to the in-duct domain (Figs. 4a and 5a), we observe results that are comparable with the ones obtained with the complete nacelle geometry (Figs. 1f and 1h). The quasi-extinction zone for BPF2 and BPF3 around $x/L = -0.7$ is still present, with a total power that remains constant from $x/L = -0.5$. When the tip line is approximated by a constant line (Figs. 4b and 5b), the acoustic pressure variations are not easily visible but the power evolution still shows some exchange of energy between BPFs. These exchange are much less pronounced than in the original duct geometry, especially at BPF2, and occur slightly earlier (around $x/L = -0.65$). When the hub line is constant (Figs. 4c and 5c), the level variations of the acoustic pressure at BPF2 are again visible and seem to be shifted towards the inlet plane. Furthermore, the wavelength is reduced when compared to the original duct case because of the decrease of the cross-section area and the increase of the average axial velocity accordingly. The evolution of acoustic power in this case therefore exhibits the exchange of energy between BPFs closer to the duct inlet (around $x/L = -0.9$), while the total power still reaches a plateau from $x/L = -0.5$. Finally and interestingly, these exchanges completely disappear in the simplest case of a straight duct (Figs. 4d and 5d). The power evolution is indeed characterized by a first part where non-linear attenuation occurs ($x/L > -0.5$) and is followed by a part ($x/L < -0.5$) where the power associated with each BPF is monotonic. We could have expected that all curves reach a plateau from $x/L = -0.5$ but the mesh is visibly insufficient to correctly propagate acoustic waves over such distances in this case where the axial velocity is much higher than in the original case (leading to significantly reduced wavelength as observed in Fig. 4d).

These results first show that the exchange of energy between BPFs observed on the ACAT1 fan stage are not caused by any acoustic reflection from the duct opening, and then, that they are closely related to the mean flow heterogeneity caused by geometry variations inside the duct.

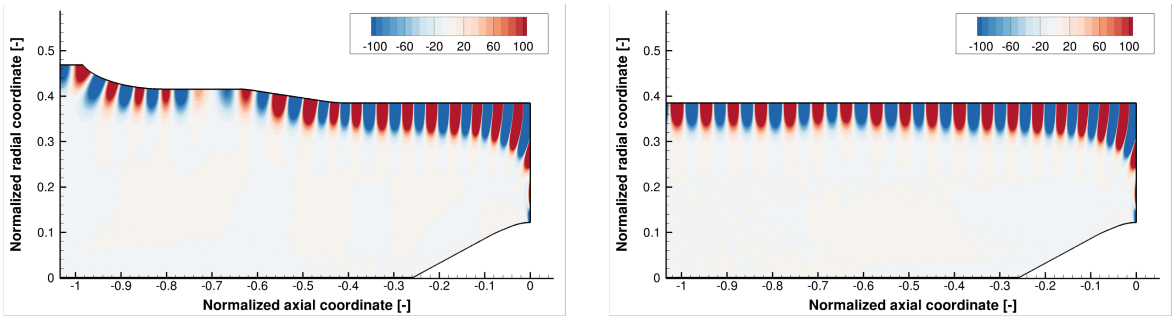

(a) Original duct geometry.

(b) Duct geometry with constant tip radius.

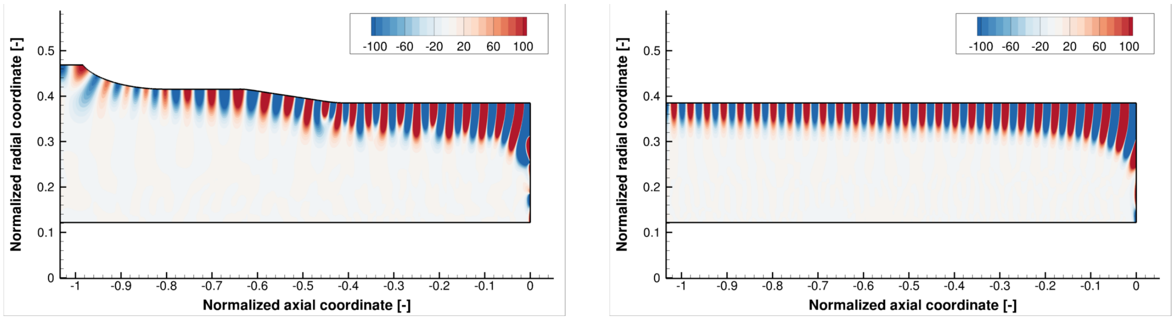

(c) Duct geometry with constant hub radius.

(d) Duct geometry with constant hub and tip radii.

Fig. 4 Contour maps of pressure real part in Pa at BPF2 on meridional plane.

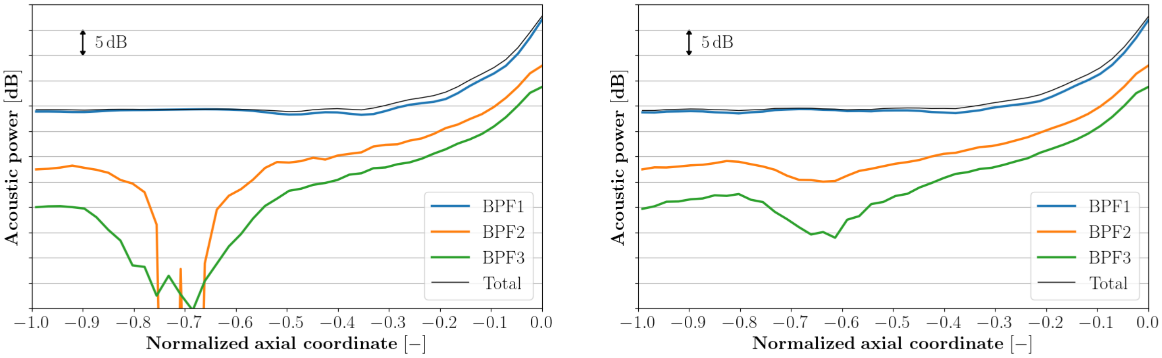

(a) Original duct geometry.

(b) Duct geometry with constant tip radius.

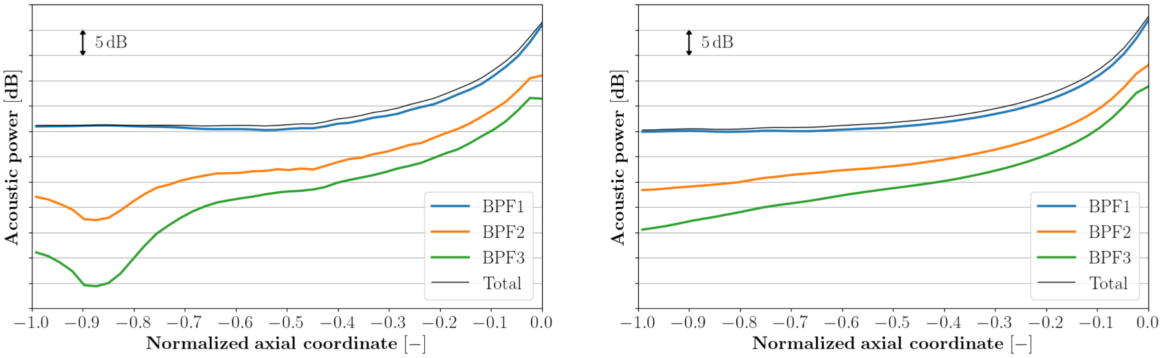

(c) Duct geometry with constant hub radius.

(d) Duct geometry with constant hub and tip radii.

Fig. 5 Axial evolution of acoustic power (total and BPF contributions).

V. Further investigations on the case with constant hub radius

The particular case with a constant hub radius (Fig. 2c) is further investigated in this section. The rationale behind this choice is that it is the most favorable case (with visible energy exchange between BPFs) for using the *sAbrinA* solver to provide additional analyses and to benchmark the previous results obtained with *elsA*. Indeed, the artificial hub avoids having very small cells close to the duct axis that could have led to long convergence times with *sAbrinA* solver which is based on an explicit time-domain integration. Note that in order to keep conciseness, the results are mainly reduced to the evaluation of the acoustic power for each BPF component in this section.

A. Effect of analytical injection

Before going into the details of the comparison between *elsA* and *sAbrinA* solvers, we first consider a simplified injection in *elsA* in order to be compliant with the source model used in *sAbrinA*. To this end, the input shock signature (illustrated in Fig. 1b) is decomposed into Fourier-Bessel modes using a semi-infinite annular duct approximation with the geometry and flow characteristics of the injection plane (as in Fig. 2d). Then, the input data is recomposed by using only the first radial order $n = 1$ of the rotor-locked modes $m = sB$ for $s = 1, 2, 3$. The density contour maps of the input data are given in Figs. 6a and 6b for the direct and recomposed data respectively while the comparison in terms of resulting acoustic power is provided in Fig. 6c. The recomposed injection from the rotor-locked modes associated with the first three BPFs necessarily leads to a smoother contour map where the shock is no more present. Nevertheless, we can observe almost no impact of this recomposition on the evolution of acoustic power inside the duct. This result shows that this simplified injection can be used in the following without having any effect on the exchange of acoustic energy between frequencies.

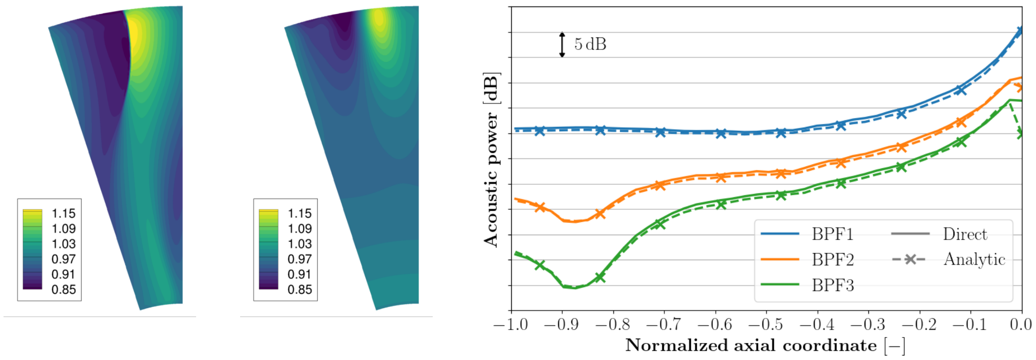

(a) Direct injection (density map in kg/m3).

(b) Analytic injection (density map in kg/m3).

(c) Acoustic power comparison (total and BPF contributions).

Fig. 6 Comparison between direct injection of shock signature from CFD and analytic injection composed with the first radial order $n = 1$ of the rotor-locked mode $m = sB$ for BPFs with $s = 1, 2, 3$.

B. Comparison between *elsA* and *sAbrinA* results

The previous *elsA* simulations obtained with the simplified injection map of Fig. 6b are compared against *sAbrinA* simulations that use the same input modes. The results in terms of evolution of acoustic power are shown in Fig. 7. As the *sAbrinA* simulations lie in the time domain and in the absolute frame, the post-processing to get these curves slightly differs from the one of *elsA* results. Indeed, a time Fourier transform is first computed in the whole volume over the last period to give access to acoustic variables at BPFs. Then, the acoustic intensity is computed over successive cross-sections using Cantrell & Hart formula [19] and is integrated to access the acoustic power. The comparison between *elsA* and *sAbrinA* results when baseline meshes are used (Fig. 7a) show a good agreement for BPF1 power level but significant differences are observed at BPF2 and BPF3. The results have been reproduced in Fig. 7b with fine meshes that comprise twice the number of points in both axial and azimuthal directions. A spectacular improvement of the comparison is thus obtained, with an excellent agreement at BPF1 and BPF2 and a similar trend at BPF3. The local decrease of acoustic power at BPF2 around $x/L = -0.85$ is particularly recovered with both solvers, as is the corresponding slight increase of BPF1 power level. At BPF3, the local decrease of power level around $x/L = -0.95$ is captured with both codes but it is more pronounced with *elsA* solver. These results confirm that there is no energy exchange with the mean flow as the base flow is uncoupled from the acoustic equations in *sAbrinA* simulations. They also show that the mechanisms that cause the exchange of acoustic energy between frequencies are highly sensitive to the mesh discretization. All results in the following (either obtained with *elsA* or *sAbrinA*) are therefore produced with fine meshes.

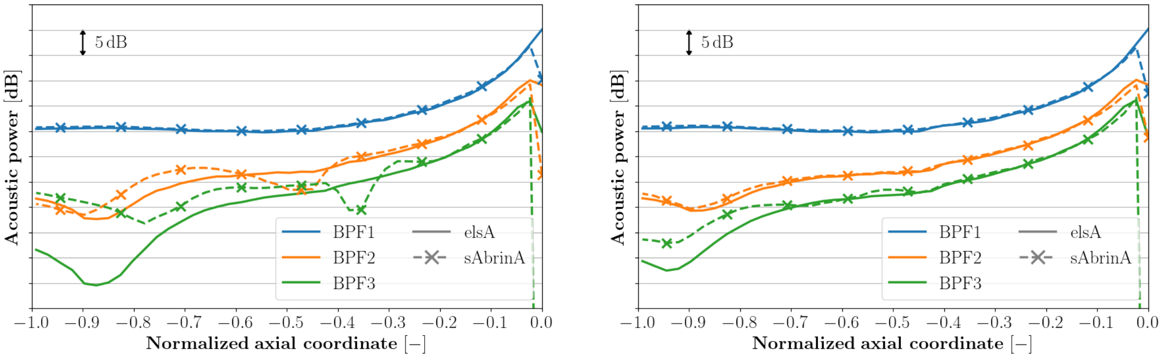

(a) Results with baseline meshes.

(b) Results with fine meshes.

Fig. 7 Comparison of axial evolution of acoustic power obtained with *elsA* and *sAbrinA*.

C. Effect of the non-linearity of governing equations

The good correspondence between *elsA* and *sAbrinA* results obtained with fine meshes (at least at BPF1 and BPF2) allows for using equivalently one or the other solver to evaluate a particular feature. This is precisely what is done here where we use the capacity of the *sAbrinA* solver to solve either the linearized or non-linearized Euler equations. The evolution of acoustic power obtained with both set of equations is provided in Fig. 8. When linear equations are considered, the acoustic power remains constant from the injection plane ($x/L = 0$) to the inlet plane ($x/L = -1$) for each BPF. This clearly shows that there is no exchange of energy between frequencies in a linear regime and it confirms that the decrease of power levels observed for $x/L > -0.5$ is effectively due to non-linear attenuation.

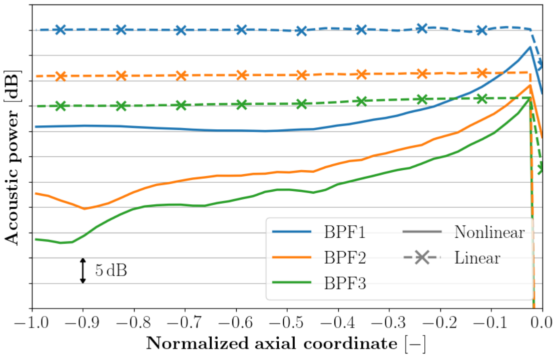

Fig. 8 Comparison of axial evolution of acoustic power obtained with *sAbrinA* with either linearized or non-linearized Euler equations.

D. Effect of frequency split at injection

This last subsection aims to evaluate the effect of separating the BPF contribution in the injected signal. In details, it consists in repeating the CAA simulation (with *elsA* and *sAbrinA* solvers) for each s^{th} harmonic of the BPF by specifying only the associated rotor-locked mode $(m = sB, n = 1)$. The resulting injection data are illustrated in Fig. 9 in terms of density contour maps. Fig. 9a is the map obtained when considering simultaneously the contributions from the first three BPFs and is the same as in Fig. 6b (but rescaled for easier comparison). The decomposition highlights a significantly higher contribution from BPF1 data.

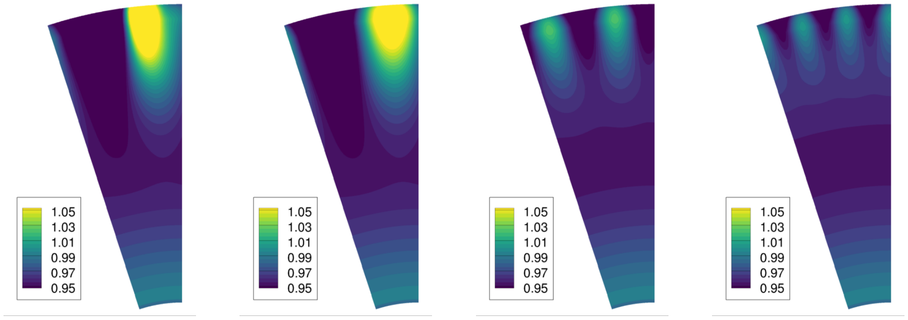

(a) Injection of all BPFs together.

(b) Injection of BPF1 only.

(c) Injection of BPF2 only.

(d) Injection of BPF3 only.

Fig. 9 Different injection data for frequency per frequency study (density map in kg/m3).

The *elsA* and *sAbrinA* power results obtained with these different injection data (with fine meshes) are plotted in Fig. 10. The decomposition of the acoustic power is here computed up to BPF6 in order to illustrate some specific features, while noting that the meshes are not meant to support such frequencies. It can first be noticed that only the harmonics of the prescribed frequency at injection are generated due to non-linear effects. As a result, all BPFs are created when injecting BPF1 alone, while only BPF2, BPF4 and BPF6 and only BPF3 and BPF6 are created when injecting BPF2 alone and BPF3 alone respectively. Interestingly, the power level associated with the prescribed frequency almost reaches a plateau from $x/L = -0.5$, while the ones of its harmonics experience important fluctuations. These fluctuations, which evidence energy exchange between frequencies, are therefore small compared to the input signal. The agreement between the power levels at the prescribed frequency obtained with *elsA* and *sAbrinA* solvers is always very good, while important differences can be observed for its harmonics. Finally, it can be noticed that the results obtained when injecting the first three BPFs together closely match the ones obtained when injecting BPF1 alone. This can be explained by an intense diffusion of BPF1 fluctuations over higher BPFs, which covers the contribution of BPF2 and BPF3 components of the input signal. This can however be surprising as, for example, the BPF2 power level obtained at the end of the duct $(x/L = -1)$ when injecting BPF2 alone is almost 5 dB higher than the one observed when injecting BPF1 alone. The presence of BPF1 in the calculation therefore seems to extract some energy from BPF2. The acoustic energy is consequently not only transferred from the prescribed frequency to its harmonics, but it is also transferred in the opposite way during the propagation.

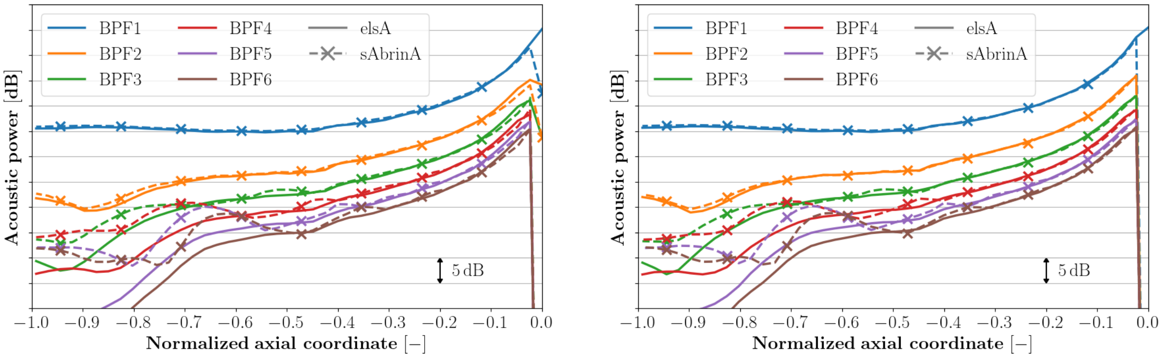

(a) Injection of all BPFs together.

(b) Injection of BPF1 only.

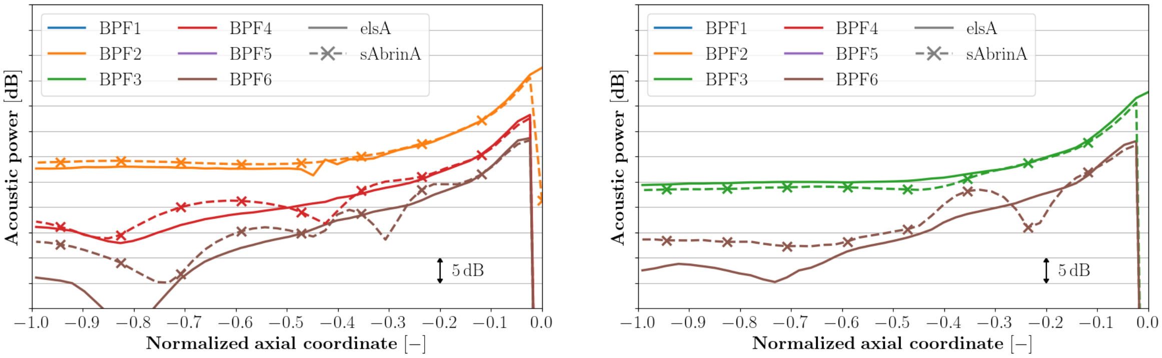

(c) Injection of BPF2 only.

(d) Injection of BPF3 only.

Fig. 10 Comparison of axial evolution of acoustic power obtained with *elsA* and *sAbrinA* for the different injections.

VI. Conclusion

In the present paper, we investigated on the origin of the variations of power levels associated with blade passing frequencies that are observed on the ACAT1 fan stage. These variations were first observed in a moderate way at nominal speed on a previous paper dedicated to the validation of a CFD/CAA chaining methodology with *elsA* solver to predict shock wave generation and propagation. But the results presented in this paper show that they are even more dramatic at a lower regime. Although using Cantrell and Hart formula for evaluating the acoustic power might be questionable in such non-linear cases, these variations occur after the total acoustic power reaches a plateau, which therefore effectively indicates an exchange of energy between frequencies. This behaviour in the case of a perfect fan without MPTs has not been reported yet in the literature to the authors knowledge and the present paper aims to bring some explanations.

The first part of the work consisted in repeating the propagation step of the CFD/CAA chaining methodology on simplified duct geometries, while keeping unchanged the input shock signature. The results show that this exchange of acoustic energy between BPFs is triggered by geometry variations and/or heterogeneous flow, and that it only vanishes when considering a straight duct (and consequently a uniform flow).

Then, more investigations on one particular geometry with constant hub radius have been conducted to benchmark the results obtained with *elsA* solver against the acoustic propagation solver *sAbrinA*, which solves the perturbation variables of the linearized or non-linearized Euler equations. A very good agreement between both solvers is obtained in non-linear mode, thus confirming that the energy exchanges occur between BPFs and not between the flow and acoustic fields (as they are uncoupled in *sAbrinA*). It is also verified with the *sAbrinA* solver that they are due to non-linearities since they disappear in linear mode. Finally, significantly different results are found, with both solvers and in a consistent way, when the input signal is prescribed frequency by frequency. In that case, the power level associated with the prescribed frequency reaches a plateau while the ones of its harmonics generated by diffusion experience important fluctuations (that nevertheless remain small compared to the input signal magnitude). Interestingly, the results obtained when injecting all frequencies together closely match the ones obtained when injecting BPF1 alone. The observed energy exchanges are therefore generated by the diffusion of BPF1 fluctuations over higher BPFs, which is of sufficiently high intensity here to cover the contribution of BPF2 and BPF3 components of the input signal.

The phenomenon reported in this paper can have a dramatic effect on the acoustic energy distribution between BPFs at the inlet plane (and consequently, in the radiated field). It is shown to be caused by a strong diffusion of the dominant frequency over its harmonics because of non-linear effects, coupled with the heterogeneity of the flow. Still, more analyses should be conducted to better understand its occurrence and intensity.

References

[1] Doherty, M., and Namgoong, H., "Impact of Turbofan Intake Distortion on Fan Noise Propagation and Generation," *22nd AIAA/CEAS Aeroacoustics Conference*, 2016. doi:https://doi.org/10.2514/6.2016-2841.

[2] Holewa, A., Guérin, S., Neuhaus, L., Danwang, L., and Huimin, T., "Tones from an Aero-Engine Fan: Comparison between Harmonic-Balance Simulation and Experiment," *22nd AIAA/CEAS Aeroacoustics Conference*, 2016. doi:https://doi.org/10.2514/6.2016-3060.

[3] Milidonis, K. F., Hynes, T., Doherty, M., and Namgoong, H., "The Effect of Steady Intake Distortion on Fan MPT Noise Under Sideline Flight Conditions," *24th AIAA/CEAS Aeroacoustics Conference*, 2018. doi:https://doi.org/10.2514/6.2018-4188.

[4] Winkler, J., Reimann, C. A., Reba, R. A., and Gilson, J., "Turbofan Inlet Distortion Noise Prediction with a Hybrid CFD-CAA Approach," *20th AIAA/CEAS Aeroacoustics Conference*, 2014. doi:https://doi.org/10.2514/6.2014-3102.

[5] Winkler, J., Reimann, C. A., Gumke, C. D., Ali, A. A., and Reba, R. A., "Inlet and Aft Tonal Noise Predictions of a Full-Scale Turbofan Engine with Bifurcation and Inlet Distortion," *23rd AIAA/CEAS Aeroacoustics Conference*, 2017. doi:https://doi.org/10.2514/6.2017-3034.

[6] Laban, M., Kok, J. C., and Brouwer, H. H., "CFD/CAA Analysis of UHBR Engine Tonal Noise," *24th AIAA/CEAS Aeroacoustics Conference*, 2018. doi:https://doi.org/10.2514/6.2018-3780.

[7] Daroukh, M., Polacsek, C., and Chelius, A., "Shock Wave Generation and Radiation from a Turbofan Engine Under Flow Distortion," *AIAA Journal*, Vol. 58, No. 2, 2020, pp. 787–801. doi:https://doi.org/10.2514/1.J058799.

[8] Behn, M., and Tapken, U., "Investigation of Sound Generation and Transmission Effects Through the ACAT1 Fan Stage using Compressed Sensing-based Mode Analysis," *25th AIAA/CEAS Aeroacoustics Conference*, 2019. doi:https://doi.org/10.2514/6.2019-2502.

[9] Daroukh, M., Polacsek, C., Thisse, J., and Nodé-Langlois, T., "Far-field shock noise prediction on the ACAT1 fan stage using a CFD/CAA chaining strategy," *29th International Congress on Sound and Vibration*, 2023.

[10] Thisse, J., Polacsek, C., Mayeur, J., Khelladi, S., Gloerfelt, X., and Lafitte, A., "Numerical Simulations of Shock-Wave Propagation in Turbofan Intakes," *22nd AIAA/CEAS Aeroacoustics Conference*, 2016. doi:https://doi.org/10.2514/6.2016-2879.

[11] Köhler, W., "The Influence of the TCS on the Circumferential Mode Distribution in the Inlet of a Fanrig (UFFA)," *Turbo Expo: Power for Land, Sea, and Air*, 2012. doi:https://doi.org/10.1115/GT2012-69762.

[12] Tapken, U., Bauers, R., Neuhaus, L., Humphreys, N., Wilson, A., Stoehr, C., and Beutke, M., "A New Modular Fan Rig Noise Test and Radial Mode Detection Capability," *17th AIAA/CEAS Aeroacoustics Conference*, 2011. doi:https://doi.org/10.2514/6.2011-2897.

[13] Redonnet, S., Manoha, E., and Sagaut, P., "Numerical simulation of propagation of small perturbations interacting with flows and solid bodies," *7th AIAA/CEAS Aeroacoustics Conference*, 2001. doi:https://doi.org/10.2514/6.2001-2223.

[14] Cambier, L., Heib, S., and Plot, S., "The Onera elsA CFD software: input from research and feedback from industry," *Mechanics & Industry*, Vol. 14, No. 3, 2013, pp. 159–174. doi:https://doi.org/10.1051/meca/2013056.

[15] Thompson, K. W., "Time Dependent Boundary Conditions for Hyperbolic Systems," *Journal of Computational Physics*, Vol. 68, No. 1, 1987, pp. 1–24. doi:https://doi.org/10.1016/0021-9991(87)90041-6.

[16] Polacsek, C., Desquesnes, G., and Reboul, G., "An equivalent-source model for simulating noise generation in turbofan engines," *Journal of Sound and Vibration*, Vol. 323, No. 3-5, 2009, pp. 697–717. doi:https://doi.org/10.1016/j.jsv.2009.01.010.

[17] Gabard, G., “Stochastic Sources of Broadband Noise for Time-Domain Simulations of Duct Acoustics,” *18th AIAA/CEAS Aeroacoustics Conference*, 2012. doi:https://doi.org/10.2514/6.2012-2239.

[18] Redonnet, S., Lockard, D., Khorrami, M., and Choudhari, M., “The non-reflective interface: an innovative forcing technique for computational acoustic hybrid methods,” *International Journal for Numerical Methods in Fluids*, Vol. 81, No. 1, 2016, pp. 22–44. doi:https://doi.org/10.1002/fld.4173.

[19] Cantrell, R. H., and Hart, R. W., “Interaction between Sound and Flow in Acoustic Cavities: Mass, Momentum, and Energy Considerations,” *The Journal of the Acoustical Society of America*, Vol. 36, No. 4, 1964, pp. 697–706. doi: https://doi.org/10.1121/1.1919047.